Strain-induced indirect-to-direct band-gap transition in bulk SnS_2

Babu Ram and Abhishek K. Singh*

Materials Research Centre, Indian Institute of Science, Bangalore 560012, India

(Received 4 October 2016; revised manuscript received 1 February 2017; published 21 February 2017)

While SnS_2 is an earth-abundant large-band-gap semiconductor material, the indirect nature of the band gap limits its applications in light harvesting or detection devices. Here, using density functional theory in combination with the many-body perturbation theory, we report indirect-to-direct band-gap transition in bulk SnS_2 under moderate, 2.98% uniform biaxial tensile (BT) strain. Further enhancement of the BT strain up to 9.75% leads to a semiconductor-to-metal transition. The strain-induced weakening of the interaction of the in-plane orbitals modifies the dispersion as well as the character of the valence- and the conduction-band edges, leading to the transition. A quasiparticle direct band gap of 2.17 eV at the Γ point is obtained at 2.98% BT strain. By solving the Bethe-Salpeter equation to include excitonic effects on top of the partially self-consistent GW_0 calculation, we study the dielectric functions, optical oscillator strength, and exciton binding energy as a function of the applied strain. At 2.98% BT strain, our calculations show the relatively high exciton binding energy of 170 meV, implying strongly coupled excitons in SnS_2. The effect of strain on vibrational properties, including Raman spectra, is also investigated. The Raman shift of both in-plane (E^1_{2g}) and out-of plane (A_{1g}) modes decreases with the applied BT strain, which can be probed experimentally. Furthermore, SnS_2 remains dynamically stable up to 9.75% BT strain, at which it becomes metallic. A strong coupling between the applied strain and the electronic and optical properties of SnS_2 can significantly broaden the applications of this material in strain-detection and optoelectronic devices.

DOI: 10.1103/PhysRevB.95.075134

I. INTRODUCTION

Layered metal dichalcogenides (LMDs) have attracted immense interest because of their unique electronic, optical, electrochemical, and catalytic properties [1–10]. Most of these properties emerge from the intensively rich and anisotropic electronic structure, adding to the unprecedented range of functionalities known for any particular class of materials. Depending on the metals or chalcogens, LMDs can be semiconductors, semimetals, metals, superconductors, and insulators [11–19]. Among the LMDs, SnS_2 is a semiconducting material with an indirect band gap of 2.3 eV [20–22]. The earth abundance of both Sn and S coupled with the environment-friendly low-cost synthesis process give bulk and nanoform SnS_2 a great advantage for large-scale industrial applications. It has been extensively used in Na-ion batteries [23], photocatalysis [24], and organic and inorganic solar cells [25]. These applications heavily rely on the electronic structure of this material. It has been shown experimentally that the band gap of SnS_2 is insensitive to the number of layers and remains indirect from monolayer to bulk [26]. While the robust layer-independent electronic structure makes this material very promising for electronic devices, the indirect band gap remains the biggest challenge for optical applications.

The functionalities of SnS_2 can be further enhanced by tailoring its electronic structure comprehensively. Recent developments in engineering electronic structures of layered materials by means of external perturbation have brought many interesting functionalities to a single LMD. The application of strain has been considered as a potential method to tune the electronic properties of MoS_2 [27–29]. The entire range of band gaps of MoS_2 can be tuned, reversibly. An indirect-to-direct band-gap transition in bilayer WSe_2 has been shown to occur upon the application of uniaxial tensile strain, which leads to a drastic enhancement in the photoluminescence intensity [30]. Monolayers of WSe_2 and MoS_2 exhibit a direct band gap [3] and show strong photoluminescence, whereas multilayers exhibit an indirect band gap and show significantly weaker photoluminescence.

Recently, even for multilayers of SnS_2, simultaneous tuning of the electronic as well as the phononic gap is achieved by applying normal compressive (NC) strain. SnS_2 was found to be stable up to 24% normal compressive strain [31]. However, it remains an indirect-band-gap semiconductor over the entire range of applied strain. Here, we report using density functional theory (DFT), an indirect-to-direct band-gap transition in bulk SnS_2 under 2.98% uniform biaxial tensile (BT) strain. Further increase in the strain leads to a semiconductor-to-metal transition at 9.75% BT strain. The structure does not show any dynamic instability over the entire range of strain, implying the strong possibility of experimental realization of these transitions. Furthermore, the Raman shifts of the E^1_{2g} and A_{1g} modes decrease with increasing BT strain. The optical properties of SnS_2 were studied by solving the Bethe-Salpeter equation (BSE) including excitonic effects on top of partially self-consistent GW_0 calculations. At 2.98% BT strain, along with a quasiparticle (QP) direct band gap of 2.17 eV, the relatively higher exciton binding energy of 170 meV is obtained. The absorption coefficient increases significantly in the visible energy regions of the electromagnetic spectrum at the band-gap transition. Interestingly, the exciton binding energy was found to be the highest among its layered counterparts such as MoS_2, $MoSe_2$, $MoTe_2$, and WS_2 and semiconductors such as GaN and ZnO, making strained SnS_2 promising for optoelectronic devices.

*abhishek@mrc.iisc.ernet.in

II. COMPUTATIONAL METHODS

We have used first-principles DFT [32] as implemented in the Vienna *ab initio* simulation package (VASP) [33,34]. Projector augmented wave [35,36] pseudopotentials were used to represent the electron-ion interactions. For band structure calculations, the Heyd-Scuseria-Ernzerhof (HSE06) hybrid functional [37–39] was used, which models the short-range exchange energy of the electrons by fractions of Fock and Perdew-Burke-Ernzerhof (PBE) exchange [33]. The addition of the Fock exchange partially removes the PBE self-interaction, which resolves the band-gap underestimation problem to a large extent. The interlayer van der Waals interaction was included through a semiempirical dispersion potential (D) to the conventional Kohn-Sham DFT energy through a pairwise force field using the Grimme's PBE-D3 method [40]. The Brillouin zone was sampled by a well-converged 9×9×9 Monkshood-Pack scheme [41] **k** grid. Structural relaxation was performed by using the conjugate-gradient method until the absolute values of the components of the Hellman-Feynman forces were converged to within 0.005 eV/Å.

In order to obtain the optimized lattice parameters of bulk SnS_2 having a hexagonal crystal structure, we performed volume optimization using the PBE-D3 by keeping the experimental $\frac{c}{a} = 1.62$ [42] constant. The in-plane lattice parameter was varied in the range from 3.69 to 4.05 Å, with an interval of 0.02 Å. In order to ensure high accuracies of forces, a strict energy convergence criterion of 1×10^{-8} eV was used to calculate the phonon dispersions using density functional perturbation theory [43]. DFT-based calculations allow us to determine the ground-state properties. In order to treat excited states, realistic QP energies are obtained by considering the Kohn-Sham eigenstates and eigenvalues as a starting point using the equation

$$E_n^{\mathrm{QP}} = E_n^{\mathrm{KS}} + \langle \psi_n^{\mathrm{KS}} | \Sigma(E_n^{\mathrm{QP}}) - V_{\mathrm{XC}} | \psi_n^{\mathrm{KS}} \rangle, \quad (1)$$

where V_{XC} and Σ are the exchange correlation potential at the DFT level and the self-energy operator term, respectively. Σ includes all the effects of exchange and correlation in a many-particle system. In the partially self-consistent scheme, the self-energy [44,45] term is written as

$$\Sigma(1,2) = iG(1,2)W_0(2,1^+), \quad (2)$$

where W_0 is a screened Coulomb interaction term. In this scheme, the iterative process of solving the GW equations does not update W, whereas the Green function (G) is determined fully self-consistently by repeated solution of the Dyson equation:

$$G(1,2) = G_0(1,2) + \int d(3,4) G_0(1,3) \sum (3,4) G(4,2). \quad (3)$$

This reduces the computational cost considerably, as it avoids the self-consistent calculation of the screened interaction W.

III. RESULTS AND DISCUSSION

SnS_2 belongs to the metal dichalcogenide (MX_2) family [20], where M and X are group IV and chalcogen elements, respectively. Hexagonal SnS_2 has a CdI_2 layered crystal structure with a space-group symmetry of $P\bar{3}m1$ [46]. The unit cell and corresponding Brillouin zone with the high-symmetry points are shown in Figs. 1(a) and 1(b). The optimized lattice parameters are $a = 3.69$ Å and $c = 5.98$ Å, which are in good agreement with experiment [42]. The Sn-S bond length ($d_{\mathrm{Sn-S}}$) is found to be 2.62 Å. The electronic band structure corresponding to unstrained SnS_2 is shown in Fig. 1(c). The valence-band maxima (VBM) and conduction-band minima (CBM) are located close to the Γ and L points, separated by an indirect band gap of 2.25 eV [47,48]. The conduction bands are more dispersive compared to the valence bands,

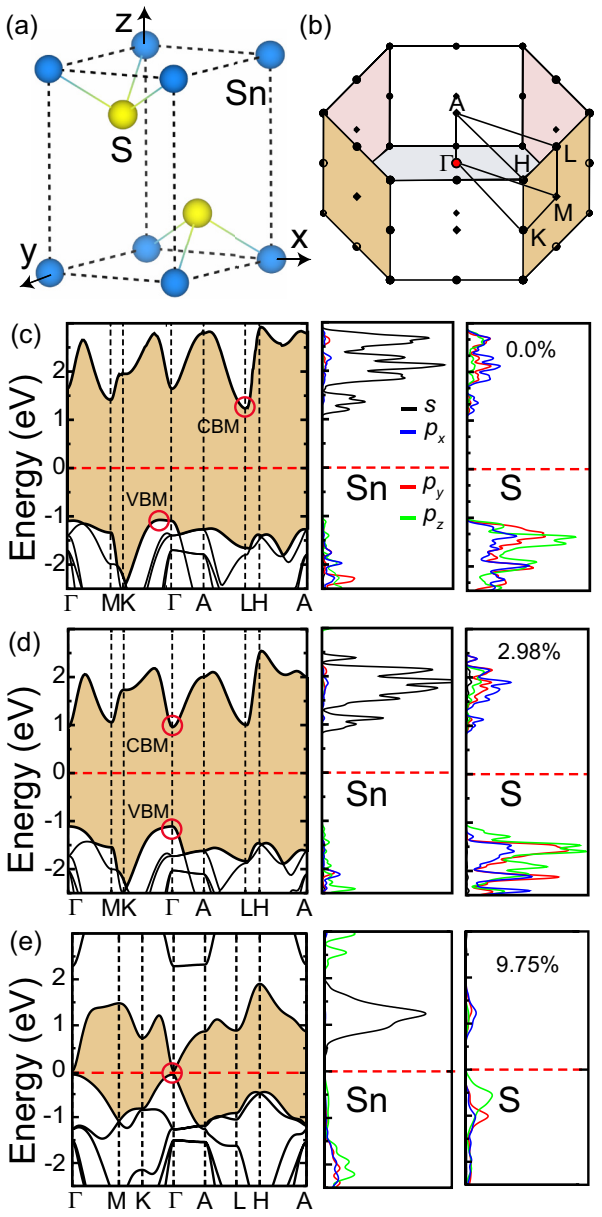

FIG. 1. (a, b) Unit cell and corresponding Brillouin zone of bulk SnS_2. (c–e) Electronic band structure and angular-momentum-resolved density of states at 0.0%, 2.98%, and 9.75% BT strain, respectively. Dashed red lines represent the Fermi level. Red circles represent the VBM and CBM.

indicating lower effective masses and higher carrier mobilities of electrons. In order to obtain the orbital contributions to the CBM and VBM, we calculate the angular-momentum-resolved density of states. Most of the orbital contribution to the VBM comes from S-$p_x/p_y/p_z$, whereas, Sn-s orbitals contribute most to the CBM, as shown in Fig. 1(c).

Strain has been used extensively to tune the electronic as well as the optical properties of materials such as MoS_2, WSe_2, SnS_2, and TiS_2 [9,30,31]. A recent experimental study also reported band-gap engineering by applying a large biaxial strain to monolayer MoS_2 [49]. This was performed by applying a pressure difference across a MoS_2 membrane suspended over a cylindrical cavity. The applied pressure difference forms a bulge and produces biaxial strain at the center of the device, which is calculated using Hencky's model [49]. These experimental results show that up to 5.6% BT strain can be applied on chemical vapor deposition–grown monolayer MoS_2 films, and this can be extended to the study of the effect of biaxial strain in mono- and multilayers of other two-dimensional materials as well. Interestingly, strain has been used to tailor the two-dimensional electron gas properties of the $LaAlO_3/SrTiO_3$ heterointerface. Experimental evidence shows that the $LaAlO_3/SrTiO_3$ heterostructure grown using pulsed-laser deposition on a $DyScO_3$ substrate results in 4% tensile strain on $LaAlO_3$, whereas on a $GdScO_3$ substrate it leads to 4.5% tensile strain on $LaAlO_3$. These strains can be used to control the two-dimensional electron gas properties at the $LaAlO_3/SrTiO_3$ interface [50]. Moreover, a recent study demonstrated that molecular beam epitaxy can be used to grow strained graphene (∼1.4% tensile strain) directly on hexagonal boron nitride. This strain is used as a route to modify the electronic properties of graphene [51]. Here, we study the effect of an applied uniform BT strain (ϵ) (defined as $\epsilon = \frac{a-a_0}{a_0}$, where, a and a_0 are lattice parameters with and without strain, respectively) on the electronic structure of SnS_2. The structure is relaxed by constraining the in-plane atomic position, while atoms are allowed to move along the out-of-plane directions. At 2.98% BT strain, the CBM shifts from the L point to the Γ point, and the VBM moves to the Γ point, causing an indirect-to-direct band-gap transition as shown in Fig. 1(d). This shift in the CBM and VBM leads to a reduction in the band gap from 2.25 eV (indirect) to 1.95 eV (direct). As in the case of unstrained SnS_2, the conduction band remains highly dispersive compared to the valence band. Upon further increasing the BT strain beyond 2.98%, the direct band gap decreases, and at 9.75% a semiconductor-to-metal transition occurs, as shown in Fig. 1(e). Interestingly, bulk SnS_2 preserves its space-group symmetry $P3m1$ even at 9.75% BT strain. Even though the material exhibits a semiconductor-to-metal transition, it happens at a very large strain and is probably difficult to achieve experimentally. However, a linear decrease in the band gap across a wide range of strains may find applications as a strain sensor. Furthermore, the BT-strain-induced indirect-to-direct band-gap transition in bulk SnS_2 was found to be independent of the choice of exchange correlation functionals such as the local density approximation, PBE, and HSE06. However, the local density approximation shows an indirect-to-direct band-gap transition at 3.35% BT strain, whereas the HSE06 and PBE functionals show the transition at 2.98%.

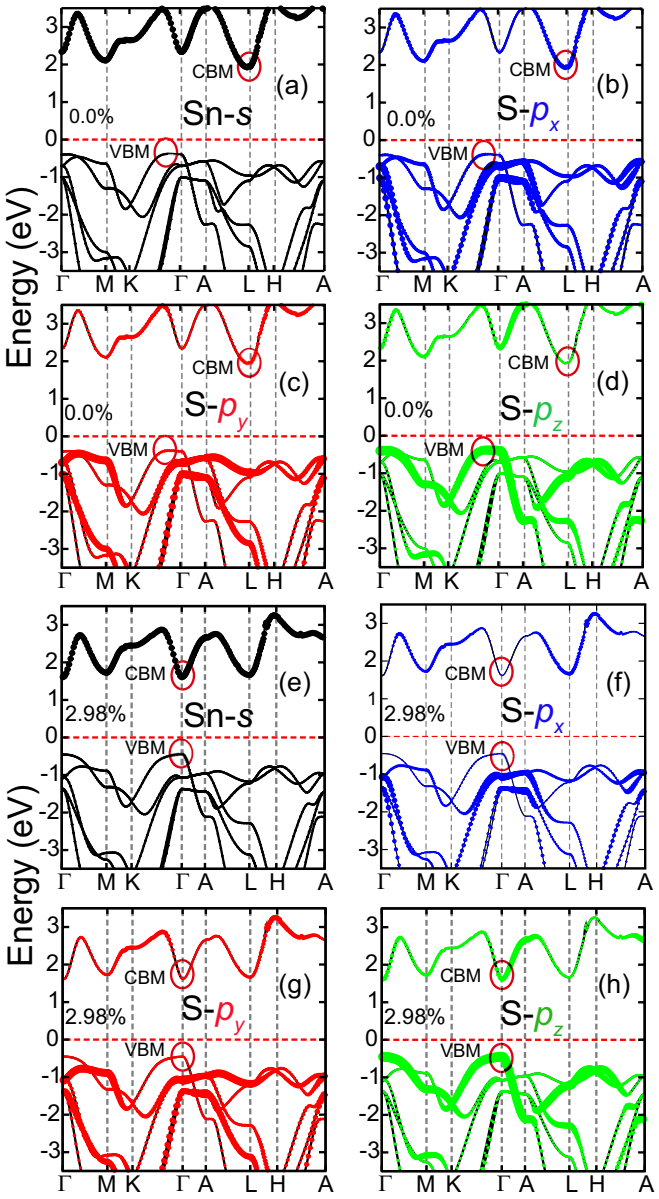

FIG. 2. Orbital-resolved band structure at 0.0% and 2.98% BT strain. Red circles represent the corresponding VBM and CBM in the band structures. The dashed red line represents the Fermi level.

In order to gain better insight into the band-gap transition in bulk SnS_2, we further study the effect of strain on orbital hybridization. For the unstrained case, the CBM originates from Sn-s orbitals, with some contribution from S-p_x/p_y orbitals, whereas the VBM originates from S-p_z orbitals, with a small contribution from S-p_x/p_y orbitals, as shown in Figs. 2(a)–2(d). At the critical BT strain of 2.98%, S-p_x/p_y orbitals move towards lower energies, so the VBM is made exclusively of S-p_z orbitals as shown in Figs. 2(f)–2(h). This leads to a shift in the VBM to the Γ point. On the other hand, the conduction-band edge at the L point also shows weakening of the interaction among Sn-s, S-p_x, and S-p_y orbitals. At the Γ point, the conduction-band edge has the maximum contribution from Sn-s and a small contribution from S-p_z orbitals. The weaker interaction between these orbitals pushes

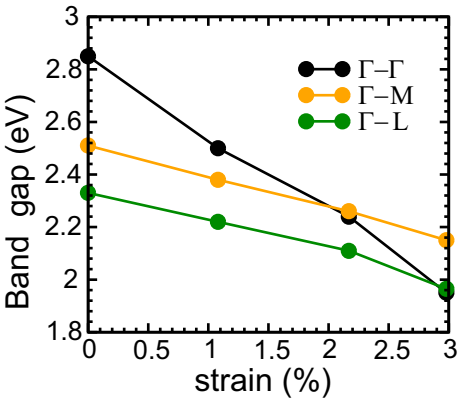

FIG. 3. Band-gap variations along the symmetric directions Γ-Γ, Γ-M, and Γ-L as a function of the BT strain.

the conduction-band edge to lower energies at the Γ point, and the CBM occurs at 2.98% BT strain, as shown in Figs. 1(d) and 2(e). Essentially, BT strain weakens the interaction of in-plane orbitals (p_x/p_y), which leads to narrowing of these bands; at the same time the out-of-plane orbitals (p_z) remain nearly unchanged. These shifts change the characteristics of the band, thereby causing an indirect-to-direct band-gap transition. As we increase the BT strain beyond 2.98%, in-plane orbitals (p_x/p_y) move farther away from the Fermi level, whereas s and p_z move closer to the Fermi level and dominate the conduction- and valence-band edges. At 9.75% BT strain, Sn-s and S-p_z orbitals cross the Fermi level, rendering it a metal, as shown in Fig. 1(e). We also studied the variation in the band gap along the different symmetry directions with the applied BT strain. It was found that variation in the band gap is relatively large along Γ-Γ as shown in Fig. 3. The contribution to the band edges at Γ comes prominently from in-plane orbitals. The hybridization of the in-plane orbitals weakens with increasing BT, which causes the band gap at Γ to vary more rapidly than the gaps at other symmetric points.

Next, we study the effect of BT strain on SnS_2 composed of a few layers. In the low-dimensional geometry of SnS_2, the effect of BT strain is found to be different than in its bulk counterpart. Even though bulk SnS_2 shows an indirect-to-direct band-gap transition at 2.98% BT strain, the band gap remains indirect up to five layers (5L) of SnS_2 at similar BT strains, as shown in Figs. 4(a)–4(d). However, the CBM and VBM, which were initially at M and close to Γ at δΓ-symmetric points, move towards Γ with an increase in the number of layers, as shown in Figs. 4(a)–4(d). We further analyze the effect of change in the surface states with the layer number at 2.98% BT strain. As we go from 2L to 5L, the contribution of surface states to the band edges decreases, however, the band gap remains indirect, as shown in Figs. 4(a)–4(d). The energy differences (ΔE) between the conduction-band edge (CBE) at Γ and the CBM at the M-symmetric point and, similarly, between the valence-band edge (VBE) at Γ and the VBM at δΓ, are plotted as a function of the inverse of the layer thickness (d^{-1}), as shown in Figs. 5(a) and 5(b). ΔE is found to vary linearly with d^{-1}. We further extrapolate this linear dependence of ΔE to the bulk limit ($d \to \infty$). The point at which the ΔE for the conduction band and valence band

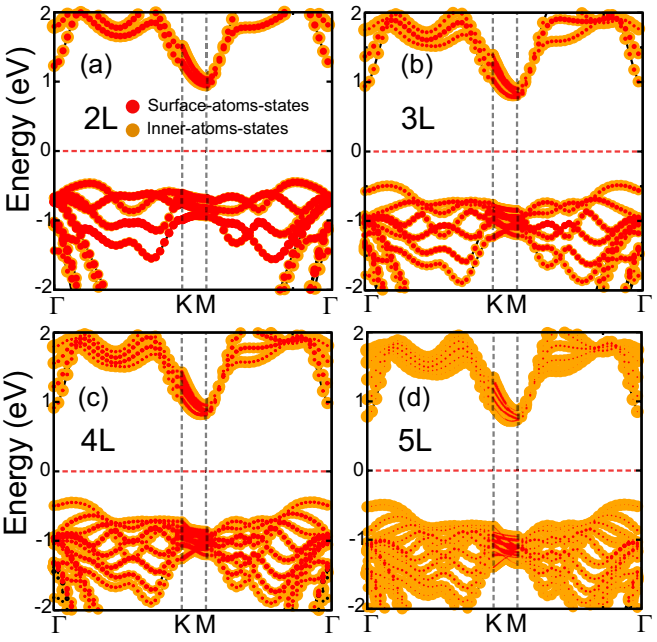

FIG. 4. Atom projected band structures at 2.98% BT strain showing variations in the surface atomic states with an increasing number of layers (2L to 5L) of SnS_2. Red and yellow spheres represent the energy states of the surface and the inner atoms. The dashed red line represents the Fermi level.

crosses the x axis ($\Delta E = 0$) represents the indirect-to-direct band-gap transition, as at this value of d^{-1} both the VBM and the CBM will be at the Γ point. For SnS_2, this transition occurs at $d^{-1} = 0.019$ Å^{-1}, which corresponds to more than 12 layers of SnS_2.

For the experimental realization of these transitions, it is of the utmost importance that the structure maintain its

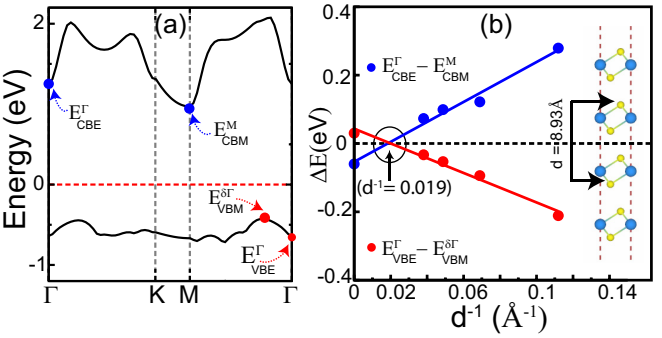

FIG. 5. (a) Dispersion of the CBM and VBM of bilayer SnS_2 at 2.98% BT strain. Blue spheres represent the conduction-band edges (CBEs) at the Γ- and M-symmetric points. Valence-band edges at Γ and δΓ are represented by red spheres. (b) The energy difference (ΔE) of the CBE at Γ (E^{Γ}_{CBE}) and the CBM at M (E^{M}_{CBM}) as a function of the inverse of the layer thickness d^{-1} is plotted by the blue line. d is the distance between the outermost sulfur atoms in 2L-SnS_2, as shown in the inset. Similarly, the energy difference between the valence-band edge (VBE) at Γ (E^{Γ}_{VBE}) and the VBM at δΓ ($E^{\delta\Gamma}_{VBM}$) as a function of d^{-1} is plotted by the red line. δΓ is the **k** point, at which the VBM of bilayer SnS_2 lies.

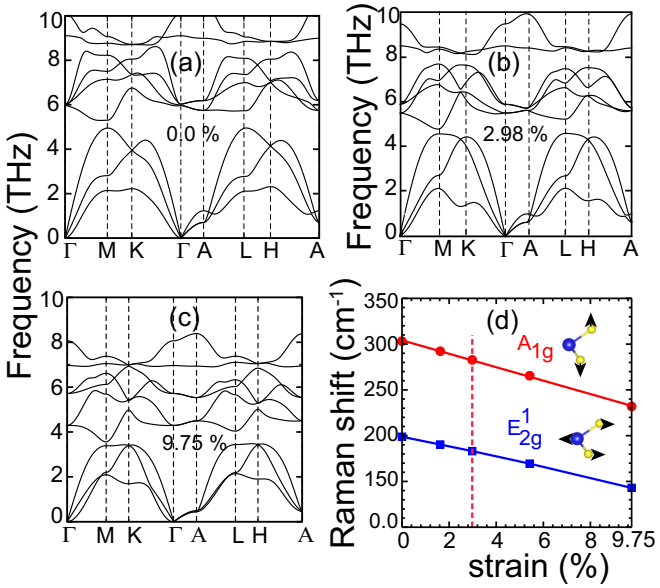

FIG. 6. (a–c) Phonon dispersion corresponding to the strain: 0.0%, 2.98%, and 9.75%. (d) Raman shift observed in the in-plane (E^1_{2g}) and out-of-plane (A_{1g}) modes with the BT strain. The modes of vibrations of Sn (blue) and S (yellow) atoms are shown.

dynamical stability under the applied BT strain. The phonon spectra of SnS_2 as a function of the BT strain do not show any negative frequency up to the transition strain as shown in Figs. 6(a)–6(c). With the BT strain, the group velocity of longitudinal acoustic (LA) modes of vibrations decreases. The group velocities of LA modes (v_{LA}) at 0.0%, 2.98%, and 9.75% BT strain are found to be 4664, 4456, and 3578 m/s, respectively. At transition strains of 2.98% and 9.75% the acoustic modes become flatter compared to the unstrained SnS_2. In addition, the characteristic phononic (acoustic-optical) gap also decreases with the BT strain. This reduction arises from the slight softening of optical modes near the Γ and L points in the phonon spectra as shown in Figs. 6(a)–6(c). With increasing BT strain, the bond lengths increase, and as a result, the interatomic force constants determining the atomic vibrational frequencies also change. Additionally, the shift in vibrational frequencies as a function of the BT strain can be used to experimentally determine the strain level in the materials through Raman spectroscopy. Next, we study Raman active in-plane (E^1_{2g}) as well as out-of-plane (A_{1g}) modes of atomic vibrations of bulk SnS_2 [52]. The Raman shift of both E^1_{2g} and A_{1g} undergo a significant reduction with the applied BT strain [Fig. 6(d)]. The A_{1g} (7.33 cm^{-1}/strain) mode varies faster than the E^1_{2g} (5.74 cm^{-1}/strain) mode, due to the stronger intralayer (Sn-S) covalent interactions. Furthermore, multilayer SnS_2 (1L to 5L) also remains dynamically stable at 2.98% BT strain.

It is well known that the presence of a direct band gap enhances the optical response of a material. In order to model and design optoelectronic devices, a study of the electronic and optical properties of the material is very important [53]. After achieving a direct band gap, we study the optical properties of SnS_2 including excitonic effects, which are essential for the understanding of photoemission, photoabsorption, and photoluminescence spectra. The interaction of excitons plays a major role in the optical responses, involving the creation of excitons without the actual addition and removal of electrons [54], and hence cannot be studied by QP calculations alone. It has been shown that the combined GW_0 and Bethe-Salpeter-equation method provides a significantly better agreement with experimental optical properties than single-particle calculations [55–57]. Therefore, we include exciton interactions via the Bethe-Salpeter equation on top of the partial self-consistent GW_0 calculations [54,56]. The Bethe-Salpeter equation for the two-particle Green's function for each excitonic state S is given by

$$\left(E^{QP}_{ck} - E^{QP}_{vk}\right)A^S_{vck} + \sum_{v'c'k'} \langle vck|K^{eh}|v'c'k'\rangle A^S_{v'c'k'} = \Omega^S A^S_{vck}, \tag{4}$$

where E^{QP}_{ck} and E^{QP}_{vk} are QP energies for the conduction-band state $|ck\rangle$ and valence-band state $\langle vk|$, respectively. A^S_{vck} and Ω^S are the exciton eigenfunction and eigenvalue for the S^{th} exciton, and K^{eh} is the electron-hole interaction term. Once the excitonic eigenvalues and eigenfunctions are obtained, the optical absorption can be calculated through the imaginary part of the dielectric function [$\varepsilon(\omega)$] as

$$\varepsilon_2(\omega) = \frac{16\pi^2 e^2}{\omega^2} \sum_S |e\langle 0|v|S\rangle|^2 \delta(\omega - \Omega^S), \tag{5}$$

where v corresponds to the velocity operator along the direction of the polarization of light represented by the polarization vector e. Using the Kramers-Kronig relation the real part of the dielectric constant $\varepsilon_1(\omega)$ can be obtained. From the dielectric function the absorption coefficient $\alpha(\omega)$ and reflectivity $R(\omega)$ can be calculated by

$$\alpha(\omega) = \sqrt{2}\omega\left[\sqrt{\varepsilon_1^2(\omega) + \varepsilon_2^2(\omega)} - \varepsilon_1(\omega)\right]^{\frac{1}{2}} \tag{6}$$

and

$$R(\omega) = \left|\frac{\sqrt{\varepsilon_1(\omega) + i\varepsilon_2(\omega)} - 1}{\sqrt{\varepsilon_1(\omega) + i\varepsilon_2(\omega)} + 1}\right|^2, \tag{7}$$

where $\varepsilon_1(\omega)$ and $\varepsilon_2(\omega)$ are the real and imaginary parts of the dielectric functions, averaged over the three crystallographic directions, respectively. The $\varepsilon_2(\omega)$ and oscillator strength (i.e., the probability of absorption or emission of electromagnetic radiation in transition between energy levels) corresponding to 0.0% and 2.98% are shown in Figs. 7(a) and 7(b).

For unstrained SnS_2 [Fig. 7(a)], the first minor peak of ε_2 originates from the optical transitions between Γ-Γ without the inclusion of electron and phonon coupling. In the case of the direct band gap at 2.98% BT strain, the first lowest energy peak originates from the single optical transition from Γ to Γ, as shown in Fig. 7(b). In Figs. 7(a) and 7(b), the oscillator strength is represented by the height of the vertical blue bars. The positions of the first bars, at 2.66 and 2.0 eV, are the direct optical gaps for 0.0% and 2.98% strained SnS_2, respectively. For unstrained bulk SnS_2, the calculated band gap at the Γ point is 2.82 eV and the corresponding exciton binding energy is 160 meV. However, the actual band gap of SnS_2 lies between L and close to the Γ-symmetric point. In order to calculate the band gap accurately using the GW_0 method, it is necessary

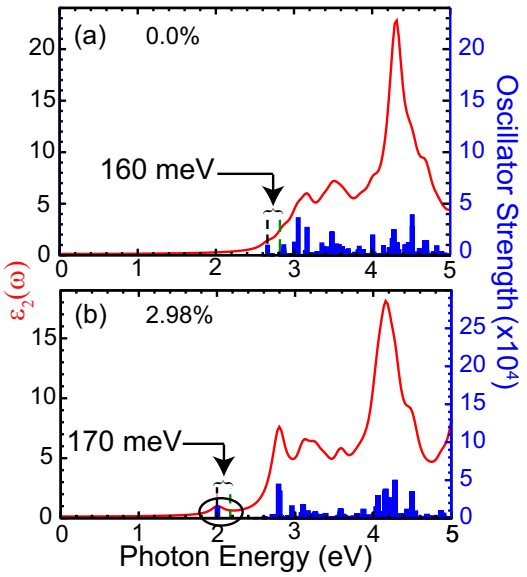

FIG. 7. Imaginary part of the dielectric constant [$\varepsilon_2(\omega)$] shown by red lines at (a) 0.0% and (b) 2.98% BT strain. Vertical blue lines represent the oscillator strength. Dashed green lines indicate a GW_0 band gap of 2.82 eV (at Γ, without including the phonon-assisted effect) and 2.17 eV at 0.0% and 2.98% strain, respectively. Dashed black lines represent the optical gaps, which are 2.66 and 2.0 eV at 0.0% and 2.98% BT strain, respectively. The difference between the position of the green and that of the black lines gives the excitonic binding energy.

to sample the band edges, which requires a denser k grid and becomes computationally expensive. Therefore, the calculated excitonic binding energy cannot be compared directly with the experimental finding for unstrained SnS_2.

A semiclassical picture of excitons obtained from the Mott-Wannier model provides intuitive insight into the causes of changes in the excitonic binding energy. The Mott-Wannier model makes use of the effective mass approximation [58], by which excitons are considered to be equivalent to hydrogen atoms, differing only in the effective masses of electron and holes and the dielectric constants of the medium. The expression for the exciton binding energy (E_b^{3D}) is given by

$$E_b^{3D} = 13.6\mu_{ex}/m_0\varepsilon^2, \quad \mu_{ex} = \frac{m_e m_h}{m_e + m_h}, \tag{8}$$

where m_0, ε, and μ_{ex} are the electron mass, static dielectric constant, and effective exciton mass, respectively. In this equation, the dielectric screening is included through the dielectric constant, whereas the effective electron and hole masses (m_e and m_h) are calculated from the curvatures of the energy bands. The band dispersion at the conduction-band edge at 2.98% BT strain decreases, whereas the band dispersion at the valence-band edge remains unchanged, leading to an overall increase in μ_{ex}. The static dielectric constant is given by $\varepsilon = \frac{2}{3}\varepsilon_{11} + \frac{1}{3}\varepsilon_{33}$, where $\varepsilon_{11} = \varepsilon_{22}$ and ε_{33} are the in-plane and transverse components of the bulk dielectric tensor, respectively. For bulk SnS_2, macroscopic ion-clamped static dielectric tensors are calculated using the HSE06 functional. For unstrained SnS_2, the values are $\varepsilon_{11} = \varepsilon_{22} = 6.58$, $\varepsilon_{33} = 4.84$, and $\varepsilon = 6.0$, whereas at 2.98% BT strain the values are $\varepsilon_{11} = \varepsilon_{22} = 6.76$, $\varepsilon_{33} = 4.75$, and $\varepsilon = 6.09$.

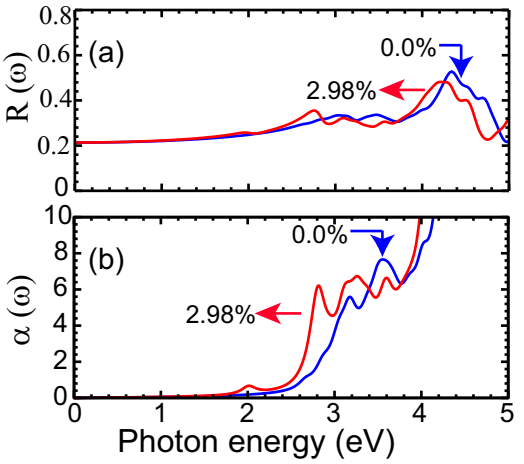

FIG. 8. Reflectivity $R(\omega)$ and absorption coefficient $\alpha(\omega)$ as a function of the photon energy (eV), where red and blue lines correspond to 0.0% and 2.98% BT strain.

According to the Mott-Wannier model, the variations in ε and μ_{ex} can lead to change in the excitonic binding energy. Interestingly, the predicted exciton binding energy corresponding to 2.98% BT strain for bulk SnS_2 is 170 meV and is very large compared to the transition-metal dichalchogenides such as MoS_2 (42 to 60 meV), $MoSe_2$ (70 meV), $MoTe_2$ (140 meV), and WS_2 (50 meV) [59–62]. Moreover, the exciton binding energy is higher than that of bulk Si (14.3 meV), GaN (28 meV), and ZnO (59 meV), respectively [63–65]. This relatively high exciton binding energy can lead to strongly coupled excitons, therefore making strained bulk SnS_2 very promising for efficient excitonic emission. Further, we study $R(\omega)$ and $\alpha(\omega)$ as a function of the photon energy as shown in Figs. 8(a) and 8(b). Both $R(\omega)$ and $\alpha(\omega)$ represent the same trend as $\varepsilon_2(\omega)$ at both 0.0% and 2.98%, as shown in Figs. 8(a) and 8(b). Once a direct band gap is achieved, the enhancement in the absorption coefficient can be seen in the visible energy range from 1.8 to 3.1 eV as shown in Fig. 8(b). The overall spectrum is red-shifted in comparison to the unstrained case. Photon absorption increases in the lower energy range compared to the unstrained SnS_2 case. Therefore, the desirable electronic and optical properties can be obtained by applying BT strain to bulk SnS_2, which will pave the way for designing novel optoelectronic and straintronic devices.

IV. CONCLUSION

In summary, we demonstrate, using density functional theory in combination with the many-body perturbation theory, an indirect-to-direct band-gap transition in bulk SnS_2 under 2.98% BT strain. Strain weakens the interaction of the in-plane orbitals, which eventually modifies the dispersion as well as the character of the valence-band edge, leading to an indirect-to-direct band-gap transition. The reduction in the direct band gap continues till a critical strain of 9.75%, at which the band gap closes at the Γ point, leading to a strain-induced semiconductor-to-metal transition. Although

the material exhibits semiconductor-to-metal transitions, it happens at very high, 9.75%, BT strain and is probably difficult to achieve experimentally. However, the decrease in the band gap across a wide range of strains may find applications for strain sensors. With increasing BT strain, the vibrational frequencies of the Raman active in-plane (E^1_{2g}) as well as out-of plane (A_{1g}) modes decrease. This strain-induced variation in the A_{1g} mode (7.33 cm^{-1}/strain) is found to be larger than that in the in-plane E^1_{2g} mode (5.74 cm^{-1}/strain). In addition, we also study the optical properties of bulk SnS_2 under applied BT strain. By solving the Bethe-Salpeter equation to include excitonic effects on top of the partially self-consistent GW_0 calculation, we found, for 2.98% BT strain, a quasiparticle band gap and excitonic binding energy of 2.17 eV and 170 meV, respectively. The exciton binding energy is found to be higher compared to those of its layered counterparts, such as MoS_2, $MoSe_2$, $MoTe_2$, and WS_2, and bulk Si, GaN, and ZnO, which could be favorable for light-emitting devices. Therefore, with the existence of a direct band gap (2.17 eV), a relatively high exciton binding energy (170 meV) coupled with the dynamic stability opens up the possibility of designing SnS_2-based novel optoelectronic devices. Our results present an important advance toward controlling the band-gap transition and the gap energy by strain engineering of bulk SnS_2 without compromising the structural integrity, which can have implications for important applications including strain detection and light-emission devices.

ACKNOWLEDGMENTS

This work was supported by DST Nanomission. The authors thank the Materials Research Centre and Super-computer Education and Research Centre, Indian Institute of Science, for the computing facilities.

[1] A. Ayari, E. Cobas, O. Ogundadegbe, and M. S. Fuhrer, J. Appl. Phys. **101**, 014507 (2007).
[2] T. Cheiwchanchamnangij and W. R. L. Lambrecht, Phys. Rev. B **85**, 205302 (2012).
[3] K. F. Mak, C. Lee, J. Hone, J. Shan, and T. F. Heinz, Phys. Rev. Lett. **105**, 136805 (2010).
[4] A. Molina-Sánchez and L. Wirtz, Phys. Rev. B **84**, 155413 (2011).
[5] W. Ho, J. C. Yu, J. Lin, J. Yu, and P. Li, Langmuir **20**, 5865 (2004).
[6] S. Wu, Z. Zeng, Q. He, Z. Wang, S. J. Wang, Y. Du, Z. Yin, X. Sun, W. Chen, and H. Zhang, Small **8**, 2264 (2012).
[7] H. P. Komsa and A. V. Krasheninnikov, Phys. Rev. B **88**, 085318 (2013).
[8] E. Benavente, M. S. Ana, F. Mendizábal, and G. González, Coord. Chem. Rev. **224**, 87 (2002).
[9] A. Samanta, T. Pandey, and A. K. Singh, Phys. Rev. B **90**, 174301 (2014).
[10] H. I. Karunadasa, E. Montalvo, Y. Sun, M. Majda, J. R. Long, and C. J. Chang, Science **335**, 698 (2012).
[11] J. Wilson and A. Yoffe, Adv. Phys. **18**, 193 (1969).
[12] K. K. Kam and B. A. Parkinson, J. Phys. Chem. **86**, 463 (1982).
[13] A. P. Nayak, S. Bhattacharyya, J. Zhu, J. Liu, X. Wu, T. Pandey, C. Jin, A. K. Singh, D. Akinwande, and J.-F. Lin, Nat. Commun. **5**, 3731 (2014).
[14] A. Kumar and P. K. Ahluwalia, Model. Simul. Mater. Sci. Eng. **21**, 065015 (2013).
[15] A. H. Reshak and S. Auluck, Phys. Rev. B **68**, 245113 (2003).
[16] D. R. Allan, A. A. Kelsey, S. J. Clark, R. J. Angel, and G. J. Ackland, Phys. Rev. B **57**, 5106 (1998).
[17] S. Nagata, T. Aochi, T. Abe, S. Ebisu, T. Hagino, Y. Seki, and K. Tsutsumi, J. Phys. Chem. Solids **53**, 1259 (1992).
[18] E. Morosan, H. W. Zandbergen, B. S. Dennis, J. W. G. Bos, Y. Onose, T. Klimczuk, A. P. Ramirez, N. P. Ong, and R. J. Cava, Nat. Phys. **2**, 544 (2006).
[19] B. Radisavljevic and A. Kis, Nat. Mater. **12**, 815 (2013).
[20] C. D. Lokhande, J. Phys. D: Appl. Phys. **23**, 1703 (1990).
[21] Y. Sun, H. Cheng, S. Gao, Z. Sun, Q. Liu, Q. Liu, F. Lei, T. Yao, J. He, S. Wei, and Y. Xie, Angew. Chem. Int. Ed. **51**, 8727 (2012).
[22] H. L. Zhuang and R. G. Hennig, Phys. Rev. B **88**, 115314 (2013).
[23] T. Zhou, W. K. Pang, C. Zhang, J. Yang, Z. Chen, H. K. Liu, and Z. Guo, ACS Nano **8**, 8323 (2014).
[24] Y. C. Zhang, Z. N. Du, S. Y. Li, and M. Zhang, Appl. Catal. B **95**, 153 (2010).
[25] F. Tan, S. Qu, J. Wu, K. Liu, S. Zhou, and Z. Wang, Nanoscale Res. Lett. **6**, 298 (2011).
[26] Y. Huang, E. Sutter, J. T. Sadowski, M. Cotlet, O. L. Monti, D. A. Racke, M. R. Neupane, D. Wickramaratne, R. K. Lake, B. A. Parkinson, and P. Sutter, ACS Nano **8**, 10743 (2014).
[27] S. Bhattacharyya and A. K. Singh, Phys. Rev. B **86**, 075454 (2012).
[28] H. Guo, T. Yang, P. Tao, Y. Wang, and Z. Zhang, J. Appl. Phys. **113**, 013709 (2013).
[29] S. Bhattacharyya, T. Pandey, and A. K. Singh, Nanotechnology **25**, 465701 (2014).
[30] S. B. Desai, G. Seol, J. S. Kang, H. Fang, C. Battaglia, R. Kapadia, J. W. Ager, J. Guo, and A. Javey, Nano Lett. **14**, 4592 (2014).
[31] B. Ram, A. Manjanath, and A. K. Singh, 2D Mater. **3**, 015009 (2016).
[32] W. Kohn and L. J. Sham, Phys. Rev. **140**, A1133 (1965).
[33] G. Kresse and J. Furthmüller, Comput. Mater. Sci. **6**, 15 (1996).
[34] G. Kresse and J. Furthmüller, Phys. Rev. B **54**, 11169 (1996).
[35] P. E. Blöchl, Phys. Rev. B **50**, 17953 (1994).
[36] G. Kresse and D. Joubert, Phys. Rev. B **59**, 1758 (1999).
[37] J. Heyd, J. E. Peralta, G. E. Scuseria, and R. L. Martin, J. Chem. Phys. **123**, 174101 (2005).
[38] B. G. Janesko, T. M. Henderson, and G. E. Scuseria, Phys. Chem. Chem. Phys. **11**, 443 (2009).
[39] J. K. Ellis, M. J. Lucero, and G. E. Scuseria, Appl. Phys. Lett. **99**, 261908 (2011).
[40] S. Grimme, J. Comput. Chem. **27**, 1787 (2006).
[41] H. J. Monkhorst and J. D. Pack, Phys. Rev. B **13**, 5188 (1976).
[42] M. Toh, K. Tan, F. Wei, K. Zhang, H. Jiang, and C. Kloc, J. Solid State Chem. **198**, 224 (2013).

[43] X. Gonze and J. P. Vigneron, Phys. Rev. B **39**, 13120 (1989).
[44] M. J. van Setten, F. Weigend, and F. Evers, J. Chem. Theory Comput. **9**, 232 (2013).
[45] M. L. Tiago, P. R. C. Kent, R. Q. Hood, and F. A. Reboredo, J. Chem. Phys. **129**, 084311 (2008).
[46] R. M. Hazen and L. W. Finger, Am. Mineral. **63**, 289 (1978).
[47] M. Y. Au Yang and M. L. Cohen, Phys. Rev. **178**, 1279 (1969).
[48] Y. Kumagai, L. A. Burton, A. Walsh, and F. Oba, Phys. Rev. Appl. **6**, 014009 (2016).
[49] D. Lloyd, X. Liu, J. W. Christopher, L. Cantley, A. Wadehra, B. L. Kim, B. B. Goldberg, A. K. Swan, and J. S. Bunch, Nano Lett. **16**, 5836 (2016).
[50] C. W. Bark, D. A. Felker, Y. Wang, Y. Zhang, H. W. Jang, C. M. Folkman, J. W. Park, S. H. Baek, H. Zhou, D. D. Fong, X. Q. Pan, E. Y. Tsymbal, M. S. Rzchowski, and C. B. Eom, Proc. Natl. Acad. Sci. USA **108**, 4720 (2011).
[51] A. Summerfield, A. Davies, T. S. Cheng, V. V. Korolkov, Y. Cho, C. J. Mellor, C. T. Foxon, A. N. Khlobystov, K. Watanabe, T. Taniguchi, L. Eaves, S. V. Novikov, and P. H. Beton, Sci. Rep. **6**, 22440 (2016).
[52] L. A. Burton, T. J. Whittles, D. Hesp, W. M. Linhart, J. M. Skelton, B. Hou, R. F. Webster, G. O'Dowd, C. Reece, D. Cherns, D. J. Fermin, T. D. Veal, V. R. Dhanak, and A. Walsh, J. Mater. Chem. A **4**, 1312 (2016).
[53] X. D. Zhang, M. L. Guo, W. X. Li, and C. L. Liu, J. Appl. Phys. **103**, 063721 (2008).
[54] G. Onida, L. Reining, and A. Rubio, Rev. Mod. Phys. **74**, 601 (2002).
[55] L. X. Benedict, E. L. Shirley, and R. B. Bohn, Phys. Rev. Lett. **80**, 4514 (1998).
[56] M. Rohlfing and S. G. Louie, Phys. Rev. Lett. **81**, 2312 (1998).
[57] R. Laskowski and N. E. Christensen, Phys. Rev. B **73**, 045201 (2006).
[58] A. Ramasubramaniam, Phys. Rev. B **86**, 115409 (2012).
[59] J. Bordas and E. A. Davis, Phys. Status Solidi **60**, 505 (1973).
[60] T. Goto, Y. Kato, K. Uchida, and N. Miura, J. Phys.: Condens. Matter **12**, 6719 (2000).
[61] H. P. Komsa and A. V. Krasheninnikov, Phys. Rev. B **86**, 241201 (2012).
[62] A. Chernikov, T. C. Berkelbach, H. M. Hill, A. Rigosi, Y. Li, O. B. Aslan, D. R. Reichman, M. S. Hybertsen, and T. F. Heinz, Phys. Rev. Lett. **113**, 076802 (2014).
[63] A. J. Read, R. J. Needs, K. J. Nash, L. T. Canham, P. D. J. Calcott, and A. Qteish, Phys. Rev. Lett. **69**, 1232 (1992).
[64] M. Dvorak, S.-H. Wei, and Z. Wu, Phys. Rev. Lett. **110**, 016402 (2013).
[65] W. Shan, B. D. Little, A. J. Fischer, J. J. Song, B. Goldenberg, W. G. Perry, M. D. Bremser, and R. F. Davis, Phys. Rev. B **54**, 16369 (1996).